RSC Advances

ROYAL SOCIETY OF CHEMISTRY

www.rsc.org/advances

Journal Name

ARTICLE

Mechanochemical Growth of Porous $ZnFe_2O_4$ Nano-flakes Thin Film as Electrode for Supercapacitor Application

Received 00th January 20xx,
Accepted 00th January 20xx

DOI: 10.1039/x0xx00000x

www.rsc.org/

M. M. Vadiyar,[a] S. C. Bhise,[a] S. K. Patil,[a] S. A. Patil,[a] D. K. Pawar,[a] A. V. Ghule,[b]* P. S. Patil[c] and S. S Kolekar[a]*

Abstract

Herein, we are reporting a simple, economic, easy to handle, scalable and reproducible mechanochemical i.e. rotational chemical bath deposition (R-CBD) approach for synthesis of well adhered nano-flakes $ZnFe_2O_4$ thin films (NFs-$ZnFe_2O_4$) with uniform morphology on stainless steel (SS) substrate, in comparison with nano-grain $ZnFe_2O_4$ thin films (NGs-$ZnFe_2O_4$) prepared using conventional CBD approach. The influence of rotation on the evolution of nano-flakes morphology in NFs-$ZnFe_2O_4$ is also investigated. The porous NFs-$ZnFe_2O_4$ thin films demonstrated excellent pseudocapacitor properties with higher specific capacitance 768 Fg^{-1} at high current density 5 mA cm^{-2}, stability upto 5000 cycles (88% retention), higher energy density (106 Wh kg^{-1}) and power density (18 kW kg^{-1}) compared to NGs-$ZnFe_2O_4$. The results were also found to be higher than those reported earlier for MFe_2O_4 based systems.

Introduction

Developing supercapacitor (SC) energy storage devices with high power density and excellent cycle stability that can fulfil continuous growing energy demand while addressing environmental concerns have attracted potential interest of the scientific community.[1-2] Supercapacitors are classified into electric double layer capacitors (EDLCs, energy is stored by charge accumulation) and pseudocapacitors (energy stored by fast reversible faradic reactions on the surface of electrode materials) based on their energy storage mechanism.[3,4] Among the several materials explored, transition metal oxides (TMOs) [5-6] such as MCo_2O_4 (M=Ni, Zn, Mg, Cu, Mn) MFe_2O_4 (M=Co, Ni, Cu and Zn)[7-8] [9-11] remain the most explored candidates as pseudocapacitive electrodes for SCs to improve the energy density and overall performance. Ferrites including magnetite of Fe_3O_4, $CoFe_2O_4$, $MnFe_2O_4$, and $CuFe_2O_4$[9,11-14] and their nanocomposites with conducting additives which could produce higher specific capacitance than typical carbonaceous materials with electric double layer capacitance have also been explored with great interest (Table T1).[15-17]

Recently, spinel transition metal oxides (AB_2O_4) have attracted great attention as promising electrode material with the use of two metal elements. Specifically, nickel cobaltite ($NiCo_2O_4$) and zinc cobaltite ($ZnCo_2O_4$) are the most studied compositions because of their higher electrochemical activity, low cost, abundant resources and environmental friendliness when compared with monometallic counterparts such as nickel oxide or cobalt oxide.[18-19] Moreover, the potential window for $NiCo_2O_4$ is only 0.4-0.6V,[17] which hardly finds practical applications. Kumbhar and coworkers reported spinel $CoFe_2O_4$ thin film prepared by using chemical bath deposition which demonstrated specific capacitance of 366 Fg^{-1} at a constant and high potential window of 1.0 V.[9,17] Particularly, among the spinel metal ferrites (MFe_2O_4) system, $ZnFe_2O_4$ is promising due to its low toxicity, high specific surface area, highly electroactive nature, good chemical and thermal stability, environmental benignity, low cost and rich abundance on Earth. Meanwhile, developing porous nanostructured thin films for SCs hold great promise considering its porosity and high surface area, which contributes in enhancement of the performance by facilitating ion transport and creating more-active reaction sites.[14] With this motivation, we report for first time a facile approach of selectively developing interconnected porous nano-flakes $ZnFe_2O_4$ (NFs-$ZnFe_2O_4$) thin films using rotational chemical bath deposition (R-CBD) and comparing with the $ZnFe_2O_4$ thin films prepared using conventional CBD having nano-grain morphology (NGs-$ZnFe_2O_4$).

Experimental

2.1 Chemicals

Unless until specified, all the chemical and reagents used in this work are AR grade chemicals. Zinc chloride ($ZnCl_2$), ferrous

[a] Analytical Chemistry and Material Science Research Laboratory, Department of Chemistry, Shivaji University, Kolhapur 416004, Maharashtra, India
E-mail: sskolekar@gmail.com
[b] Green Nanotechnology Laboratory, Department of Chemistry, Shivaji University, Kolhapur 416004, Maharashtra, India
E-mail: anighule@gmail.com
[c] Thin Film Materials Laboratory, Department of Physics, Shivaji University, Kolhapur 416 004, India
† Footnotes relating to the title and/or authors should appear here.
Electronic Supplementary Information (ESI) available: [details of any supplementary information available should be included here]. See DOI: 10.1039/x0xx00000x

chloride tetrahydrate ($FeCl_2.4H_2O$), mono-ethanolamine (MEA) and ammonia received from (Merck chemicals) were used as such for the thin film deposition.

2.2 Synthesis of NFs-$ZnFe_2O_4$ and NGs- $ZnFe_2O_4$ thin films

The $ZnFe_2O_4$ thin films were prepared by heating mixture of aqueous alkaline solutions of $ZnCl_2$ (0.1 M, 25 mL) and $FeCl_2.4H_2O$ (0.2 M, 25 mL) in a water bath maintained at 55 ^oC. The mixture of aqueous solution was first stirred for 15 min to ensure complete dissolution resulting in clear solution. This was followed by addition of 3 mL of mono-ethanolamine (MEA) as a complexing agent and dropwise addition of ammonia for adjusting the pH 10 (±0.5) to form blue coloured solution. Further, ultrasonically cleaned stainless steel substrates were immersed into the bath solution when the temperature reached 35°C and subsequently the temperature was raised to 55 ^oC. In the first case, the deposition was achieved without rotation of the stainless substrate immersed in solution bath and is referred as conventional CBD (C-CBD). In the second case, the stainless steel substrate immersed in solution bath was rotated using gear motor with speed controller during the deposition of the thin film (R-CBD). The $ZnFe_2O_4$ thin films obtained by R-CBD were studied for their morphological changes at different rotation speeds of 15, 30, 45, 55 and 65 rpm. The heterogeneous reactions that initiate on the substrates involve the adsorption of atoms when the solution reaches the super-saturation. In both the cases, the deposition was carried out for 3 h to ensure completion of reaction. Increase in thicknesses of the $ZnFe_2O_4$ thin films was noted with increasing deposition time. The $ZnFe_2O_4$ thin film deposited substrates were further removed from the bath and washed thoroughly with double distilled water and subsequently by ethanol. The thin films were further dried in oven at 60 °C for 5 h in air atmosphere and later annealed at 550 °C to ensure decomposition of organic matter and transformation of hydroxide phase into crystalline phase.[20]

2.3 Material Characterizations

Both NFs-$ZnFe_2O_4$ and NGs- $ZnFe_2O_4$ thin film samples were characterized for their structure, composition, thermal stability, morphology and supercapacitive properties. The crystalline quality, phase identification are characterized by XRD (Bruker, D2-Phaser X-ray diffractometer) with $CuK_{\alpha 1}$ (λ=1.5406 Å) radiation in the range 20˚-80˚. The TGA thermograms were obtained using TG Analyzer (SDT Q600 V20.9 Build 20) in the temperature range from 25 to 800 ^oC, with heating rate 10 $^oC\ min^{-1}$ in air atmosphere. Raman spectra were obtained using Horiba Jobin Yvon with Lab RAM HR system at room temperature using a 532 nm solid state laser as excitation source. The surface morphology of the $ZnFe_2O_4$ thin films was characterized by scanning electron microscopy (SEM) using JSM-6360 JEOL SEM and Hitachi, S-4700. X-ray photoelectron spectroscopy (XPS-PHI 5300 PHI USA) was used to study the chemical composition and oxidation state. BET surface area analysis and pore size analysis was performed using Quantachrome NOVA1000e, USA.

2.4 Electrochemical Characterization

The NFs-$ZnFe_2O_4$ and NGs- $ZnFe_2O_4$ thin film samples were explored for supercapacitor application by constructing the cell involving three electrode system. The cyclic voltammetry (CV) curves were obtained at different scan rates of 10 to 100mVs^{-1}. Charge-discharge study as function of varying current densities from 5 to 30 mA cm^{-2} and electrochemical impedance spectroscopy (EIS) in the frequency range from 1 Hz to 100 kHz was performed using CHI 608E electrochemical analyzer.

2.5 Construction of a supercapacitor cell

The electrochemical cell with three electrode system was composed of graphite (G) as a current collector, silver-silver chloride (Ag/AgCl) as reference electrode and prepared NFs-$ZnFe_2O_4$/NGs-$ZnFe_2O_4$ thin film on stainless steel (SS) substrate as working electrode, while aqueous 3M KOH solution was used as electrolyte as shown in following equations 1 and 2.[21]

SS/NFs-$ZnFe_2O_4$/3M KOH (aq)/Ag/AgCl/G ----- 1

SS/NGs-$ZnFe_2O_4$/3M KOH (aq)/Ag/AgCl/G ----- 2

Results and discussion

3.1 Formation mechanism and reaction of NFs-$ZnFe_2O_4$ and NGs-$ZnFe_2O_4$ thin films

The fabrication process of the NFs-$ZnFe_2O_4$ and NGs-$ZnFe_2O_4$ thin films are shown in Scheme 1. First, NFs-$ZnFe_2O_4$ thin films were grown on stainless steel substrates *via* R-CBD based on the mechanical clockwise rotation of the substrate at varying rotations, however, sample prepared using 55 rpm is taken as representative sample. On the other hand, NGs-$ZnFe_2O_4$ thin films were obtained using conventional CBD in which substrate was fixed (0 rpm). The rotation of substrate enhances the mobility of molecules due to collision, probability of interaction and reaction; hence it increases the number nucleation sites with fine particle size. The fast dissociation rate of mono-ethanolamine (MEA) determines the kinetics of the reaction between dissociated OH and corresponding metal precursors. In comparison, the sample with the fixed substrate (0 rpm) produces nano-grains morphology as a result of slow movement of atoms decreasing the rate of dissociation of mono-ethanolamine (MEA) and metal precursors, followed by aggregation.[22]

Scheme 1 Schematic showing the formation of NFs-$ZnFe_2O_4$ and NGs-$ZnFe_2O_4$ thin films.

The deposition of $ZnFe_2O_4$ thin films follows three step reactions. First step involves the nucleation process in which complexation of Zn^{2+} and Fe^{2+} with complexing agent MEA takes place. The second step involves super-saturation of the solution because of increased ratio of ionic product and solubility product, which influences the growth of nuclei and thickness of the film. The third step is the termination step of the reaction which retards the growth of the film. The overall reaction is presented in the reaction mechanism 1. The reactions (1) and (2) depict the formation of metal hydroxides from the corresponding metal complexes. The reaction (3) shows the oxidation of ferrous hydroxide to geothite (iron oxyhydroxide). The fourth reaction presents the reaction of zinc hydroxide and geothite to form crystalline zinc ferrite thin films on the SS substrates by removing water while annealing temperature of 550 ^oC is set.[22]

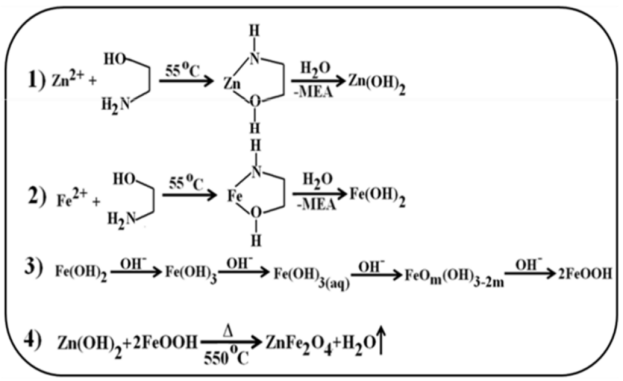

Reaction Mechanism 1 of $ZnFe_2O_4$ thin films

3.2 Morphological, thermal, structural, surface area and elemental analysis of $ZnFe_2O_4$ thin films.

In order to clarify the formation mechanism of the NFs-$ZnFe_2O_4$ and NGs- $ZnFe_2O_4$ thin films on stainless steel, the products grown at various rotations speed were investigated by SEM.

Fig. 1 SEM images obtained from different rotation speeds (a) 0 rpm (b) 15 rpm (c) 30 rpm (d) 45 rpm (e) 55 rpm and (f) 65 rpm thin films.

Initially the substrates are fixed (0 rpm) in the solution which gives nano-grain like morphology as clearly observed on the surface of stainless steel (Fig. 1(a)). When the rotation was applied to substrates, as a result of the mechanical force the nano-grains were found to be transformed into interconnected nano-flakes like morphology. The initial rotation speed of the 15 rpm shows mixed growth of nano-flakes and nano-grains (Fig. 1(b)) which confirms the transformation of nano-grain structure into nano-flakes. When the rotation speed increased to 30 rpm the shape and size of nano-grains are partially converted into uniformly adhered nano-flakes (Fig. 1(c)). The rotation speed was further extended to 45 rpm which shows well defined porous networks of the nano-flakes as shown in Fig. 1(d). For the further confirmation, the rotation speed was increased to 55 and 65 rpm (Fig. 1(e) and (f)) which showed nearly same morphology and demonstrated the growth of uniform size (~25 nm) nano-flakes. NFs-$ZnFe_2O_4$ film did not detach from the stainless steel, even after higher rotation speeds, suggesting that the film was strongly adhered to the substrate. This strong adhesion was presumably due to the maximum reaction sites obtained on the conducting substrates by rotation. Among the different rotation speeds we use 0 rpm and 55 rpm for the further characterization and electrochemical measurement study.

Fig. 2(a) and 2(b) (along with insets) show SEM images of NFs-$ZnFe_2O_4$ thin films obtained at 55 rpm rotation speed and NGs-$ZnFe_2O_4$ thin films obtained from 0 rpm rotation, respectively. The difference in morphology can be attributed to the trapping of MEA agent within the structures as a result of rotation of the substrate, which hindered attainment of equilibrium during deposition and growth of $ZnFe_2O_4$ thin films, unlike in case of conventional CBD with fixed substrate.[23]

Fig. 2 SEM images of (a) NFs-$ZnFe_2O_4$ and (b) NGs-$ZnFe_2O_4$. (c) TGA thermograms and (d) XRD patterns of NFs-$ZnFe_2O_4$ and NGs-$ZnFe_2O_4$ thin films.

The observed significant variation in surface morphology and porous nature, probably as a result of trapping MEA and/or water molecules and observed thermal stability lead to curiosity, which is further justified from thermogravimetry analysis (TGA, 25-800 °C, 10 °C min^{-1} in air atmosphere) of sample scooped from NFs-$ZnFe_2O_4$ and NGs-$ZnFe_2O_4$ thin films (Fig. 2(c)). The TGA thermogram of NFs-$ZnFe_2O_4$ showed weigh loss in steps of 4.5 (H_2O), 13.1, 3.7 and 3.4% as a function of temperature with total weight loss of 24.7% attributing to the loss of H_2O[24] and decomposition of MEA[25] and oxidation of carbonaceous matter[25] trapped into the pores of nano-flakes structures. On the other hand, the TGA thermogram of NGs-$ZnFe_2O_4$ showed weigh loss in steps of 1.3 (H_2O), 2.6, 2.3 and 1.4% as a function of temperature with total weight loss of 7.6% attributing to the loss of H_2O[24] and decomposition of MEA[25] and oxidation of carbonaceous matter[25] trapped into the voids of nano-granular structures. The difference in weight loss indicates that the MEA and subsequent carbonaceous matter trapped in the pores of nano-flakes is more than in voids of nano-grains, justifying the difference in porosity and in agreement with observed morphology. Furthermore, the crystal structure and phase formation were characterized by X-ray diffraction (XRD). The XRD spectra recorded from both NFs-$ZnFe_2O_4$ and NGs-$ZnFe_2O_4$ thin films (Fig. 2(d)) confirmed the crystal structure to be spinel cubic, however, the spectrum obtained from NGs-$ZnFe_2O_4$ thin films showed presence of trace amount of α-Fe_2O_3. In Fig. 2(d), the peaks corresponding to bare stainless steel are marked as SS and the peaks at 2θ of 30.0° (220), 35.3° (311), 44.7° (400), 53.3° (422), 56.6° (511), 62.3° (440), and 74.7° (622) could be attributed to cubic spinel phase $ZnFe_2O_4$ (JCPDS 11-0325). The additional peak at 33.4° in NGs-$ZnFe_2O_4$ could be assigned to the α-Fe_2O_3 obtained from unreacted hydroxides of iron.[3] The NFs-$ZnFe_2O_4$ and NGs- $ZnFe_2O_4$ thin films were characterized by Raman spectrophotometer and the resulting spectra is as shown in Fig. 3. Both the spectra revealed that NGs-$ZnFe_2O_4$ and NFs-$ZnFe_2O_4$ thin films have cubic structure that belongs to the space group O_h^7(Fd3m)[26-27] and have five first-order Raman active modes (A_{1g} + E_g + $3T_{2g}$), and all these modes were observed at ambient conditions. In the cubic spinel including ferrites, the modes at above 600 cm^{-1} mostly correspond to the motion of oxygen in tetrahedral AO_4 groups. So the mode at 613 cm^{-1} can be reasonably considered to have A_{1g} symmetry. The other four first-order Raman modes at 299 (E_g), 171, 412, 501 cm^{-1} (T_{2g}) corresponds to NGs-$ZnFe_2O_4$ and NFs-$ZnFe_2O_4$ thin films respectively. The all four first-order Raman modes (E_g + $3T_{2g}$) representing the characteristics of the octahedral sites (BO_6). The obtained results were in good agreement with the literature reports.[24,28]

Fig. 3 Raman spectra of NFs-$ZnFe_2O_4$ and NGs-$ZnFe_2O_4$ thin films.

The difference in porosity was further confirmed by Brunauer–Emmett–Teller (BET) multipoint surface area and Barrett–Joyner–Halenda (BJH) pore size distribution analysis (Fig. 4(a) and (b)) of NFs-$ZnFe_2O_4$ (120 m^2g^{-1}; the average pore distribution ~1.7nm) and NGs-$ZnFe_2O_4$ (67 m^2g^{-1}, ~ 2.5nm).[28]

Fig. 4 N2 adsorption-desorption isotherms and pore size (nm) distribution (insets) of synthesized (a) NFs-$ZnFe_2O_4$ and (b) NGs-$ZnFe_2O_4$ thin films.

Fig. 4 (a) and (b) shows N_2 adsorption-desorption isotherms of synthesized NFs-$ZnFe_2O_4$ and NGs-$ZnFe_2O_4$ thin films, respectively, and inset of corresponding pore size distributions (nm). For both cases, the isotherms shows discrete hysteresis loop starting from P/Po ~ 0.45 indicating the presence of inter-connected as well as structurally open pores. The corresponding pore size distributions were calculated from the desorption part of the isotherms. Mesoporous nature with a combination of narrow and broad size distribution have been observed in both cases indicating coexistence of structural pores as well as inter-connected pores. BET multipoint surface area values are calculated to be 123 and 67 m^2g^{-1}, respectively, for NFs-$ZnFe_2O_4$ and NGs-$ZnFe_2O_4$ nanostructures. A significant increase in the pore volume in NFs-$ZnFe_2O_4$ compared to the NFs-$ZnFe_2O_4$ can be related to presence of a large number of voids in its unique *nano-flakes* morphology.[29-30]

The elemental composition and chemicals state in NFs-$ZnFe_2O_4$ and NGs-$ZnFe_2O_4$ thin films was confirmed by XPS survey spectra (Fig. 5(a)) showing the presence of Zn, Fe and O with adventitious C confirming the formation of $ZnFe_2O_4$.[31] Fig. 5(b) shows core level high resolution spectra of Zn_{2p} wherein peaks corresponding to binding energy at 1021.58, 1021.38 and 1044.80, 1044.65 eV corresponding to Zn $2p_{3/2}$ and Zn $2p_{1/2}$, respectively, were observed for NFs-$ZnFe_2O_4$ and NGs-$ZnFe_2O_4$ samples. The oxidation state of the Zn was noted to be +2 in the prepared thin films. Fig. 5(c) shows high resolution spectra of Fe_{2p} demonstrating the binding energy peaks at 711.46 and 710.90 for NFs-$ZnFe_2O_4$ and NGs-$ZnFe_2O_4$ thin films, respectively, due to Fe $2p_{3/2}$. The peak appearing at 725.15 and 724.97 eV could be attributed to Fe $2p_{1/2}$ for NFs-$ZnFe_2O_4$ and NGs-$ZnFe_2O_4$ thin films. The observed results were in good agreement with the earlier reports indicating the oxidation state of Fe to be +3. Furthermore, Fig. 5(d) shows high resolution O_{1s} spectra with binding energy of 530.24 and 529.15 eV for NFs-$ZnFe_2O_4$ and NGs-$ZnFe_2O_4$, respectively, due to the lattice oxygen (O^{2-}) in the prepared $ZnFe_2O_4$ thin film. The observed results show that there is small difference in binding energies of Fe_{2p}, Zn_{2p} and O_{1s} between the NFs-$ZnFe_2O_4$ and NGs-$ZnFe_2O_4$ thin films. Binding energies of the NFs-$ZnFe_2O_4$ thin films are found to shift towards larger value as compared with NGs-$ZnFe_2O_4$ thin film sample because the arrangement of nano-flakes contain maximum number of reactive sites due to the mechanical force, while the nano-grains structures is expected to have minimum number of reactive sites.[28-29,32]

Fig. 5 (a) Full XPS survey spectrum (b) High-resolution XPS spectra for Zn_{2p}, (c) High-resolution XPS spectra for Fe_{2p} (d) High-resolution XPS spectra for O_{1s} of NFs-$ZnFe_2O_4$ (Black line) and NGs- $ZnFe_2O_4$ (Red line) thin films.

3.3 Supercapacitor study of NFs-$ZnFe_2O_4$ and NGs- $ZnFe_2O_4$ thin films.

The supercapacitor application was studied by using electrochemistry, wherein three electrodes cell system was constructed. Fig. 6(a) shows cyclic voltammetry (CV) curves obtained from NFs-$ZnFe_2O_4$ and NGs-$ZnFe_2O_4$ thin films at 10 mVs^{-1} scan rate, wherein redox peaks were observed within the negative potential range from -1.4 to -0.3 V due to the Faradaic redox reactions related to M-O/M-O-OH, where M refers to Zn or Fe demonstrating pseudocapacitive behavior.[33] The pseudocapacitive behaviour of $ZnFe_2O_4$ thin film is due to the intercalation and de-intercalation between Fe^{3+} and electrolytic K^+ ion onto the porous electrode surface. Further, galvanostatic charge-discharge measurements from NFs-$ZnFe_2O_4$ and NGs-$ZnFe_2O_4$ thin films (Fig. 6 (b)) were carried out within the potential window of -1.3 to -0.3 V vs. Ag/AgCl at 5 mA cm^{-2} current density, which showed maximum specific capacitance of 768 Fg^{-1} and 534 Fg^{-1}, respectively, which is higher than earlier reports (Table 1). The capacitance value was derived from the discharge curves using equation 3 and 4.

$$C = \frac{I \times \Delta t}{\Delta V} \quad \text{---------- 3}$$

$$Cs = \frac{C}{m} \quad \text{---------- 4}$$

Where Cs is specific capacitance, I is the constant discharge current, m is the active mass (0.0008 g) of working electrode, ΔV is the voltage range and Δt is the discharging time, respectively. Cycle stability of both NFs-$ZnFe_2O_4$ and NGs-$ZnFe_2O_4$ electrodes were checked by repeating the charge discharge tests between potential window of -1.3 to -0.3V with current density of 15 mA cm^{-2}. Initially, decrease in the specific capacitance with increase in cycle number upto 500 cycles is observed and is attributed to the expansion/contraction of electroactive species. However, beyond 500 cycles the specific capacitance was found to stable showing capacitance retention of 88% and 86% after 5000 cycles for NFs-$ZnFe_2O_4$ and NGs-$ZnFe_2O_4$, respectively as shown in Fig. 6(c). This result is marginally better than that previously reported for MFe_2O_4 based electrodes at high current density (Table T1).

Table T1. Summary of electrochemical measurements reported in recent papers using MFe_2O_4 (M=Co, Cu, Mn, Fe) as supercapacitor electrodes

The electrochemical impedance spectra (EIS) with Nyquist plots are shown in Fig. 6(d). The impedance spectra obtained from NFs-$ZnFe_2O_4$ andNGs-$ZnFe_2O_4$ were observed to be similar showing a quasi-semicircle at a higher frequency region and a spike at lower frequency. The bulk solution resistance (R_e), charge transfer resistance (R_{ct}) and Warburg resistance (Z_w) showed negligible difference in both samples at lower frequency. The R_{ct} values were noted to be ~3.0 Ω, indicating a very facile charge transfer in NFs-$ZnFe_2O_4$ and NGs-$ZnFe_2O_4$ thin films. The small R_e value shown in Fig. 6 (d) inset, further reveals good electrical conductivity of NFs-$ZnFe_2O_4$ and NGs-$ZnFe_2O_4$ thin films.[34]

Fig. 6 (a) Cyclic voltammograms at 10 mVs^{-1} scan rate (b) Galvanostatic charge-discharge curves at 5 mA cm^{-2} (c) Cycle stability up to 5000 cycles (d) Nyquist plots obtained from NFs-$ZnFe_2O_4$ and NGs-$ZnFe_2O_4$ thin films.

The CV curves were also recorded at varying scan rate 10, 20, 40, 60, 80 and 100 mVs^{-1} from NFs-$ZnFe_2O_4$ (Fig. 7(a)) and NGs-$ZnFe_2O_4$ (Fig.7(b)) thin films. The increase in scan rate increases the area under the curve which gives redox peaks at maximum current density. Hence the specific capacitance decreases. To further confirm the supercapacitive properties of NFs-$ZnFe_2O_4$ and NGs-$ZnFe_2O_4$ thin films as electrode material, the charge-discharge measurements were also carried out within the potential window -1.3 to -0.3 V vs. Ag/AgCl at different current densities 5 to 30 mA cm^{-2} for NFs-$ZnFe_2O_4$, while 5 to 20 mA cm^{-2} for NGs-$ZnFe_2O_4$ as shown in Fig.

7(c) and (d), respectively. The calculated specific capacitance for both films are 768, 391, 214, 183 Fg^{-1} and 534, 245,137, 95 Fg^{-1} at current densities 5, 10, 20, 30 mA cm^{-2} and 5, 10, 15, 20 mA cm^{-2}, respectively. It can be observed that the calculated specific capacitances of both the electrodes of $ZnFe_2O_4$ thin films decreased along with the increase in current density (Fig. 7(e)). At high current density, the low diffusion of electrolytic cation (K^+) reduces the specific capacitance. The ionic motion in the electrolyte is always limited by diffusion because of the time constraint during the high-rate of charge-discharge process, and only the outer active surface is utilized for charge storage.

Fig. 7 (a) and (b) Cyclic Voltammograms (CV) at 10, 20, 40, 60, 80, 100 mVs^{-1} scan rates (c) and (d) Galvanostatic charge-discharge (GCD) curves of at 5, 10, 20, 30 mA cm^{-2} and 5, 10, 15, 20 mA cm^{-2} in 3M KOH electrolyte and (e) and (f) plot of current density (mA cm^{-2}) vs. Specific capacitance (Fg^{-1}) and Ragone plot of energy density vs. power density for NFs-$ZnFe_2O_4$ (Black line) and NGs-$ZnFe_2O_4$ (Red line) nanostructured thin films.

Finally, the energy density ($Whkg^{-1}$) and power density ($kWkg^{-1}$) were calculated using following equations 5 and 6.

$$E = \frac{0.5Cs\times(\Delta V)^2}{3.6} \ Whkg^{-1} \text{ -------- 5}$$

$$P = \frac{E\times 3600}{\Delta t} \ kWkg^{-1} \text{ ---------- 6}$$

Where E is energy density, P is the power density, ΔV is the voltage range and Δt is the discharging time, respectively. Ragone plot (Fig. 7(f)) shows decrease in energy density with the increasing power density. The energy density of NFs-$ZnFe_2O_4$ and NGs-$ZnFe_2O_4$ was found to decrease from 106 to 25 $Whkg^{-1}$ and 74 to 13 $Whkg^{-1}$, respectively, while power density increased from 3.12 to 18.71 $kWkg^{-1}$ and 3.57 to 14.30 $kWkg^{-1}$, respectively.[35] The observed values are higher than those reported earlier when compared with similar systems composed of $MnFe_2O_4$/graphene (5 $Whkg^{-1}$), $ZnFe_2O_4$/$Ni(OH)_2$ (33 $Whkg^{-1}$) and Fe_2O_3 (105 $Whkg^{-1}$).[36] The enhanced specific capacitance and energy density is attributed to the high ionic conductivity of the aqueous electrolyte and synergistic effect between the electrodes.

Conclusions

In summary, the present work demonstrates the development of a simple, economic, easy to handle, scalable and reproducible soft mechanochemical (R-CBD) deposition technique for the deposition of binder free porous spinel NFs-$ZnFe_2O_4$ thin films showing excellent performance as promising electrode materials in supercapacitor. The NFs-$ZnFe_2O_4$ thin films (768 Fg^{-1}) showed better pseudocapacitive behavior than NGs-$ZnFe_2O_4$ thin films (534 Fg^{-1}) in 3M KOH aqueous electrolyte, within the potential window (-1.3 to -0.3V) at current density of 5 mA cm^{-2} and are higher than those reported earlier for MFe_2O_4.The capacitance retention was noted to be 88% even after 5000 cycles demonstrating good cycle stability. Therefore, employing R-CBD as soft chemical synthetic route to assemble porous electrodes demonstrating high specific capacitance may open new avenue to engineer other promising materials for improved electrochemical properties with great promise in energy storage device applications.

Notes and references

1. T. Brezesinski, J. Wang, S. H. Tolbert and B. Dunn, *Nat Mater.,* 2010, **9**, 146-151.
2. Z. S. Wu, Y. Sun, Y. Z. Tan, S. Yang, X. Feng and K. Müllen, *J. Am. Chem. Soc.,* 2012, **134**, 19532-19535.
3. X. Yao, C. Zhao, J. Kong, H. Wu, D. Zhou and X. Lu, *Chem. Commun.,* 2014, **50**, 14597-14600.
4. Z. C. Yang, C. H. Tang, Y. Zhang, H. Gong, X. Li and J. Wang, *Sci. Rep.,* 2013, **3**, 2595.
5. H. Wang, J. Guo, C. Qing, D. Sun, B. Wang and Y. Tang, *Chem. Commun.,* 2014, **50**, 8697-8700.
6. D. Zhao, Y. Xiao, X. Wang, Q. Gao and M. Cao, *Nano Energy,* 2014, **7**, 124-133.
7. Q. Zhou, J. Xing, Y. Gao, X. Lv, Y. He, Z. Guo and Y. Li, *ACS Appl. Mater. Interfaces,* 2014, **6**, 11394-11402.
8. S. Wang, J. Pu, Y. Tong, Y. Cheng, Y. Gao and Z. Wang, *J. Mater. Chem. A,* 2014, **2**, 5434-5440.
9. V. S. Kumbhar, A. D. Jagadale, N. M. Shinde and C. D. Lokhande, *Appl. Surf. Sci.,* 2012, **259**, 39-43.
10. J. L. Gunjakar, A. M. More, K. V. Gurav and C. D. Lokhande, *Appl. Surf. Sci.,* 2008, **254**, 5844-5848.
11. J. Chen, K. Huang and S. Liu, *Electrochim. Acta,* 2009, **55**, 1-5.
12. S. L. Kuo and N. L. Wu, *Electrochem. Solid-State Lett.,* 2005, **8**, A495-A499.
13. M. Zhu, D. Meng, C. Wang and G. Diao, *ACS Appl. Mater. Interfaces,* 2013, **5**, 6030-6037.
14. Y. Zhang and Z. Guo, *Chem. Commun.,* 2014, **50**, 3443-3446.
15. M. C. Liu, L. B. Kong, C. Lu, X. M. Li, Y. C. Luo and L. Kang, *ACS Appl. Mater. Interfaces,* 2012, **4**, 4631-4636.
16. S. Vijayakumar, S. Nagamuthu and G. Muralidharan, *ACS Sustainable Chem. Eng.,* 2013, **1**, 1110-1118.
17. Z. Y. Yu, L. F. Chen and S. H. Yu, *J. Mater. Chem. A,* 2014, **2**, 10889-10894.
18. B. Guan, D. Guo, L. Hu, G. Zhang, T. Fu, W. Ren, J. Li and Q. Li, *J. Mater. Chem. A,* 2014, **2**, 16116-16123.
19. G. Zhang and X. W. Lou, *Sci. Rep.,* 2013, **3**, 1470.
20. D. K. Pawar, S. M. Pawar, P. S. Patil and S. S. Kolekar, *J. Alloys Comp.,* 2011, **509**, 3587-3591.
21. D. K. Pawar, J. S. Shaikh, B. S. Pawar, S. M. Pawar, P. S. Patil and S. S. Kolekar, *J Porous Mater.,* 2012, **19**, 649-655.
22. L. Wang, H. Ji, S. Wang, L. Kong, X. Jiang and G. Yang, *Nanoscale,* 2013, **5**, 3793-3799.
23. Z. Yu, Z. Cheng, S. R. Majid, Z. Tai, X. Wang and S. Dou, *Chem. Commun.,* 2015, **51**, 1689-1692.
24. M. Wang, Z. Ai and L. Zhang, *The J. Phys. Chem. C,* 2008, **112**, 13163-13170.
25. G. Nam, B. Kim, Y. Park, S. Park, J. Moon, D. Y. Kim, S. O. Kim and J. Y. Leem, *J Mater. Chem. C,* 2014, **2**, 9918-9923.
26. K. Mukherjee and S. B. Majumder, *Sens. Actuators B: Chemical,* 2012, **162**, 229-236.
27. O. Akhavan, A. Meidanchi, E. Ghaderi and S. Khoei, *J. Mater. Chem. B,* 2014, **2**, 3306-3314.

28. H. Lv, L. Ma, P. Zeng, D. Ke and T. Peng, *J. Mater. Chem.,* 2010, **20**, 3665-3672.
29. A. Shanmugavani and R. K. Selvan, *RSC Adv.,* 2014, **4**, 27022-27029.
30. R. Indhrajothi, I. Prakash, M. Venkateswarlu and N. Satyanarayana, *RSC Adv.,* 2014, **4**, 44089-44099.
31. X. Hou, X. Wang, L. Yao, S. Hu, Y. Wu and X. Liu, *New J. Chem.,* 2015, **39**, 1943-1952.
32. Y. Zhang, Q. Shi, J. Schliesser, B. F. Woodfield and Z. Nan, *Inorg. Chem.,* 2014, **53**, 10463-10470.
33. J. W. Lee, A. S. Hall, J.-D. Kim and T. E. Mallouk, *Chem. Mater.,* 2012, **24**, 1158-1164.
34. Z. Wang, X. Zhang, Y. Li, Z. Liu and Z. Hao, *J. Mater. Chem. A,* 2013, **1**, 6393-6399.
35. Q. Tang, W. Wang and G. Wang, *J. Mater. Chem. A,* 2015, **3**, 6662-6670.
36. J. Hao, W. Yang, Z. Zhang, B. Lu, B. Zhang and J. Tang, *Electrochim. Acta,* 2015, **152**, 13-18.

Journal Name

ARTICLE

Figure and table caption

Scheme 1 Schematic showing the formation of NFs-$ZnFe_2O_4$ and NGs-$ZnFe_2O_4$ thin films.

Fig. 1 SEM images of $ZnFe_2O_4$ thin films obtained from different rotation speeds (a) 0 rpm (b) 15 rpm (c) 30 rpm (d) 45 rpm (e) 55 rpm and (f) 65 rpm.

Fig. 2 SEM images of (a) NFs-$ZnFe_2O_4$ and (b) NGs-$ZnFe_2O_4$ thin films (c) TGA thermograms and (d) XRD patterns of NFs-$ZnFe_2O_4$ and NGs-$ZnFe_2O_4$ thin films.

Fig. 3 Raman spectra of NFs-$ZnFe_2O_4$ and NGs-$ZnFe_2O_4$ thin films.

Fig. 4 N_2 adsorption-desorption isotherms and pore size (nm) distribution (insets) of (a) NFs-$ZnFe_2O_4$ and (b) NGs-$ZnFe_2O_4$ thin films.

Fig. 5 (a) Full XPS survey spectrum (b) High-resolution XPS spectra for Zn2p, (c) High-resolution XPS spectra for Fe2p (d) High-resolution XPS spectra for O1s of NFs-$ZnFe_2O_4$ (Black line) and NGs- $ZnFe_2O_4$ (Red line) thin films.

Fig. 6 (a) Cyclic voltammograms at 10 mVs^{-1} scan rate (b) Galvanostatic charge-discharge curves at 5 mA cm^{-2} (c) Cycle stability up to 5000 cycles (d) Nyquist plots obtained from NFs-$ZnFe_2O_4$ and NGs-$ZnFe_2O_4$ thin films.

Fig. 7 (a) and (b) Cyclic Voltammograms (CV) at 10, 20, 40, 60, 80, 100 mVs^{-1} scan rates (c) and (d) Galvanostatic charge-discharge (GCD) curves of at 5, 10, 20, 30 mA cm^{-2} and 5, 10, 15, 20 mA cm^{-2} in 3M KOH electrolyte and (e) and (f) plot of current density (mA cm^{-2}) vs. Specific capacitance (Fg^{-1}) and Ragone plot of energy density vs. power density for NFs-$ZnFe_2O_4$ (Black line) and NGs- $ZnFe_2O_4$ (Red line) nanostructured thin films.

Table T1 Summary of electrochemical measurements reported in recent papers using MFe_2O_4 (M=Co, Cu, Mn, Fe) as supercapacitor electrodes.

Figures

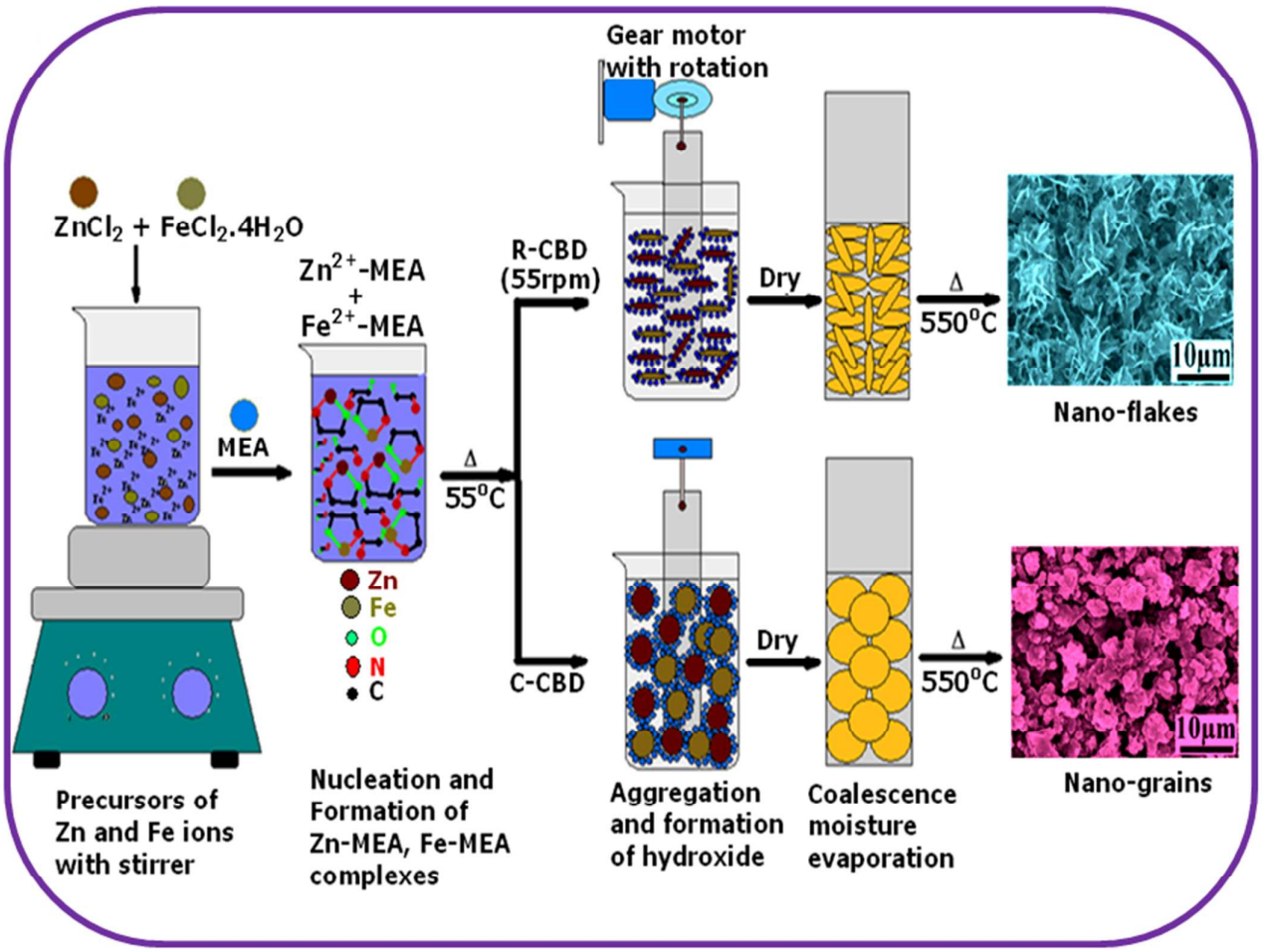

Scheme 1 Schematic showing the formation of NFs-$ZnFe_2O_4$ and NGs-$ZnFe_2O_4$ thin films.

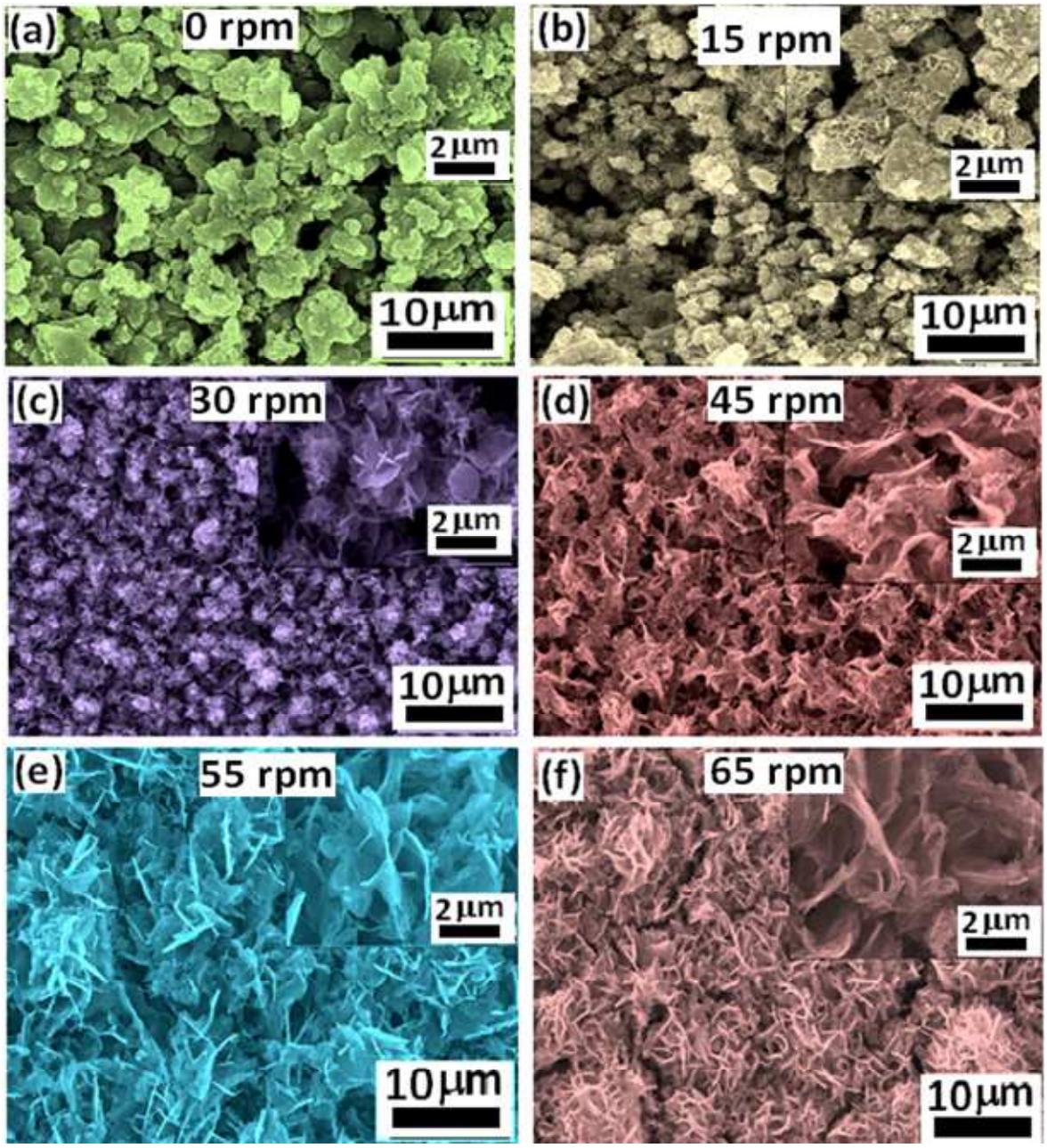

Fig. 1 SEM images of $ZnFe_2O_4$ thin films obtained from different rotation speeds (a) 0 rpm (b) 15 rpm (c) 30 rpm (d) 45 rpm (e) 55 rpm and (f) 65 rpm.

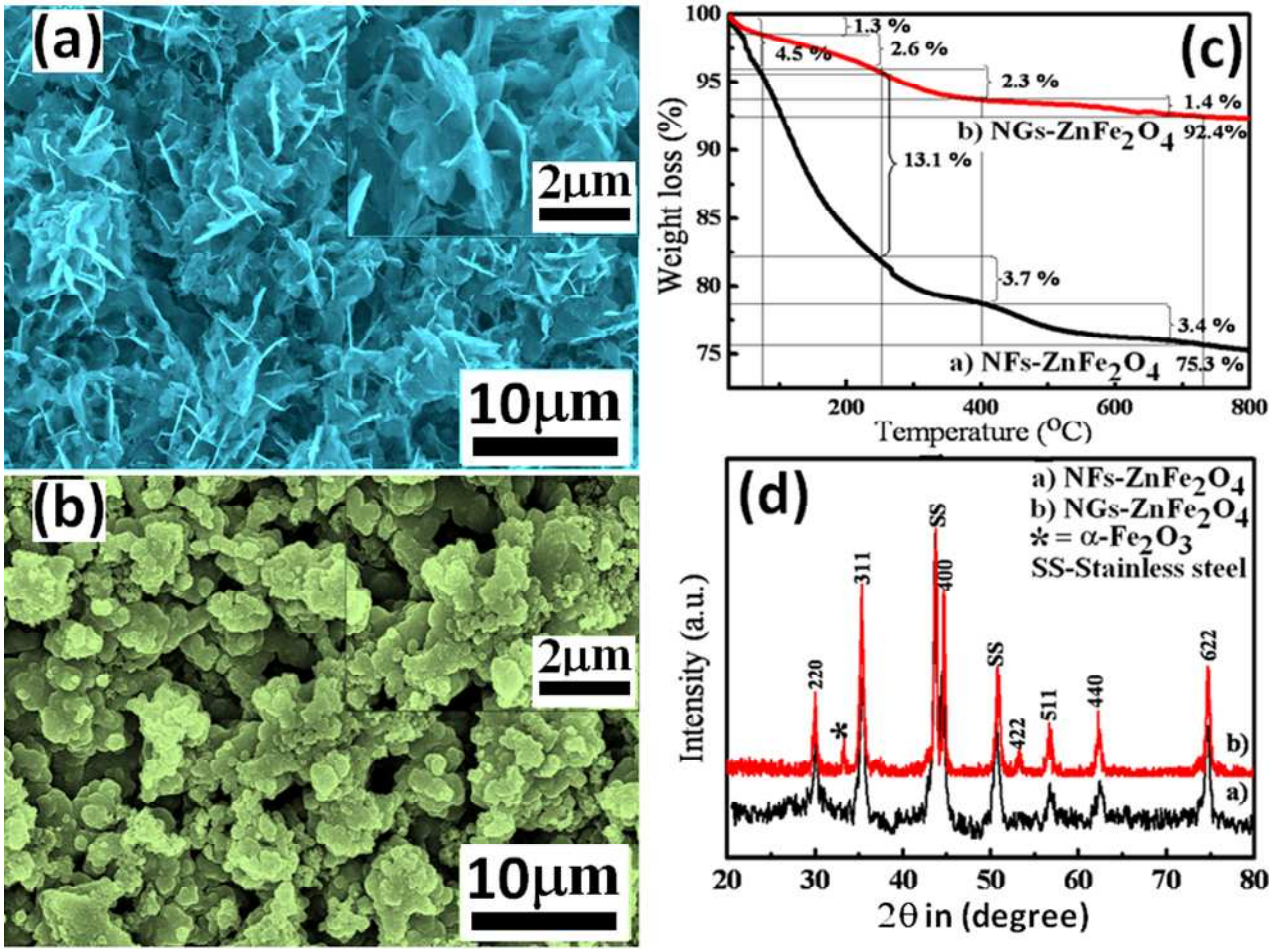

Fig. 2 SEM images of (a) NFs-$ZnFe_2O_4$ and (b) NGs-$ZnFe_2O_4$ (c) TGA thermograms and (d) XRD patterns of NFs-$ZnFe_2O_4$ and NGs-$ZnFe_2O_4$ thin films.

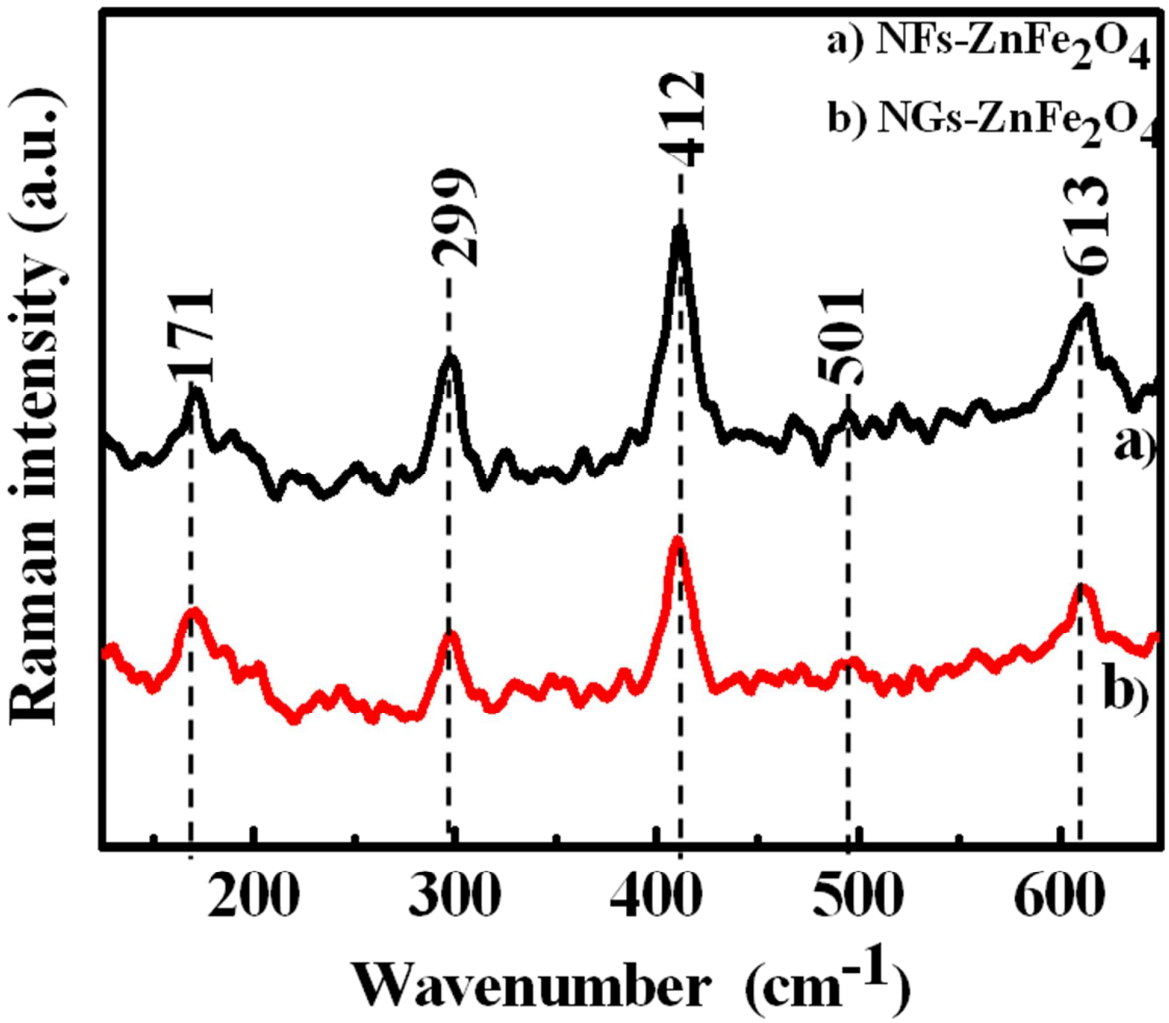

Fig. 3 Raman spectra of NFs-$ZnFe_2O_4$ and NGs-$ZnFe_2O_4$ thin films.

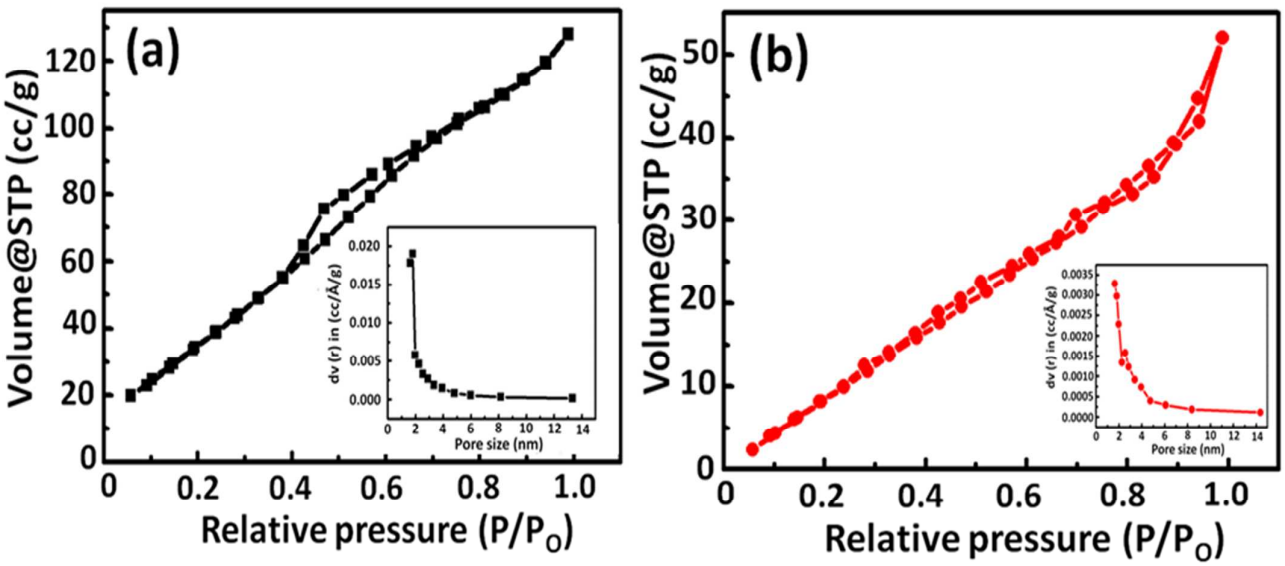

Fig. 4 N_2 adsorption-desorption isotherms and pore size (nm) distribution (insets) of NFs-$ZnFe_2O_4$ and NGs-$ZnFe_2O_4$ thin films.

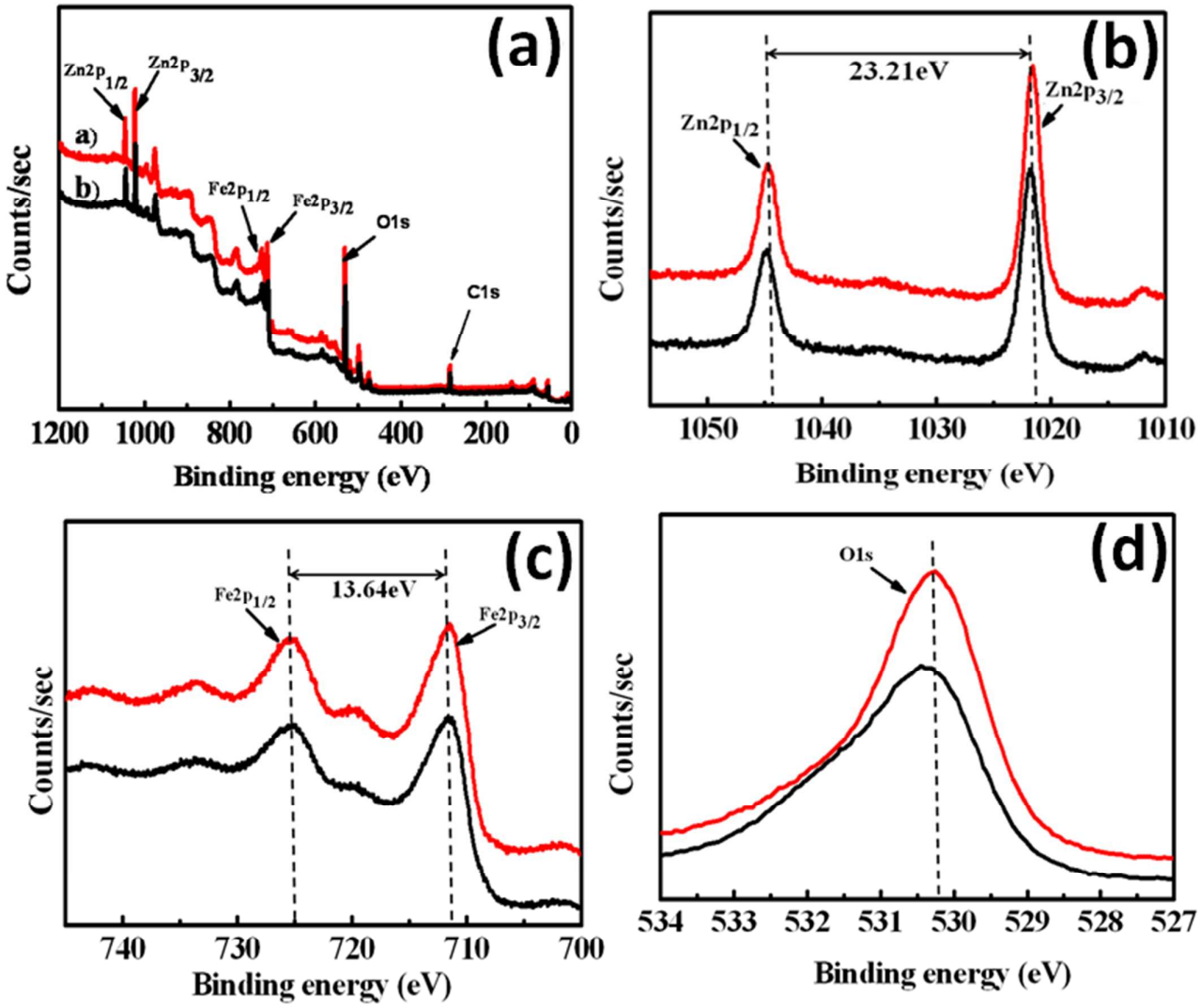

Fig. 5 (a) Full XPS survey spectrum (b) High-resolution XPS spectra for Zn2p, (c) High-resolution XPS spectra for Fe2p (d) High-resolution XPS spectra for O1s of NFs-$ZnFe_2O_4$ (Black line) and NGs-$ZnFe_2O_4$ (Red line) thin films.

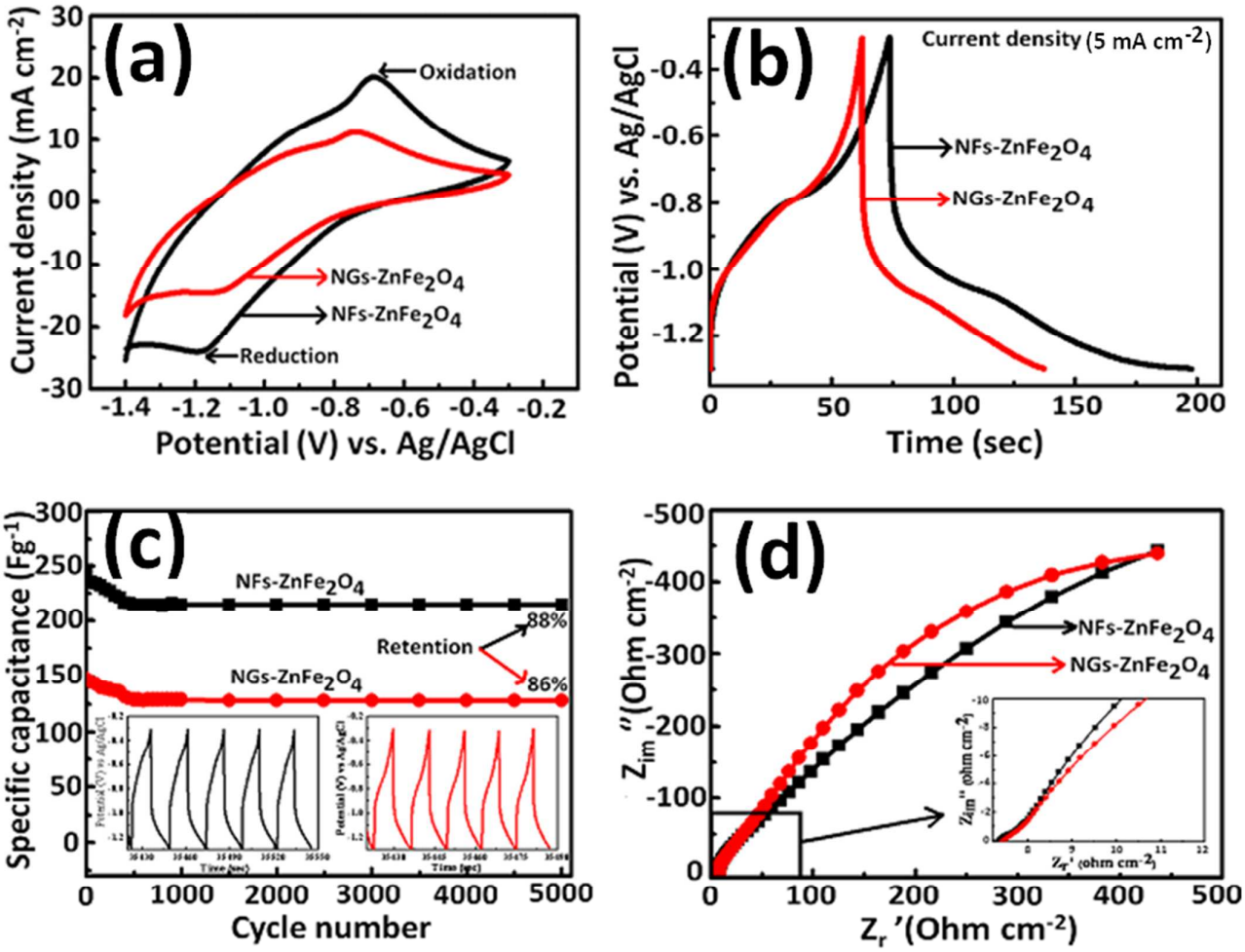

Fig. 6 (a) Cyclic voltammograms at 10 mVs^{-1} scan rate (b) Galvanostatic charge-discharge curves at 5 mA cm^{-2} (c) Cycle stability up to 5000 cycles (d) Nyquist plots obtained from NFs-$ZnFe_2O_4$ and NGs-$ZnFe_2O_4$ thin films.

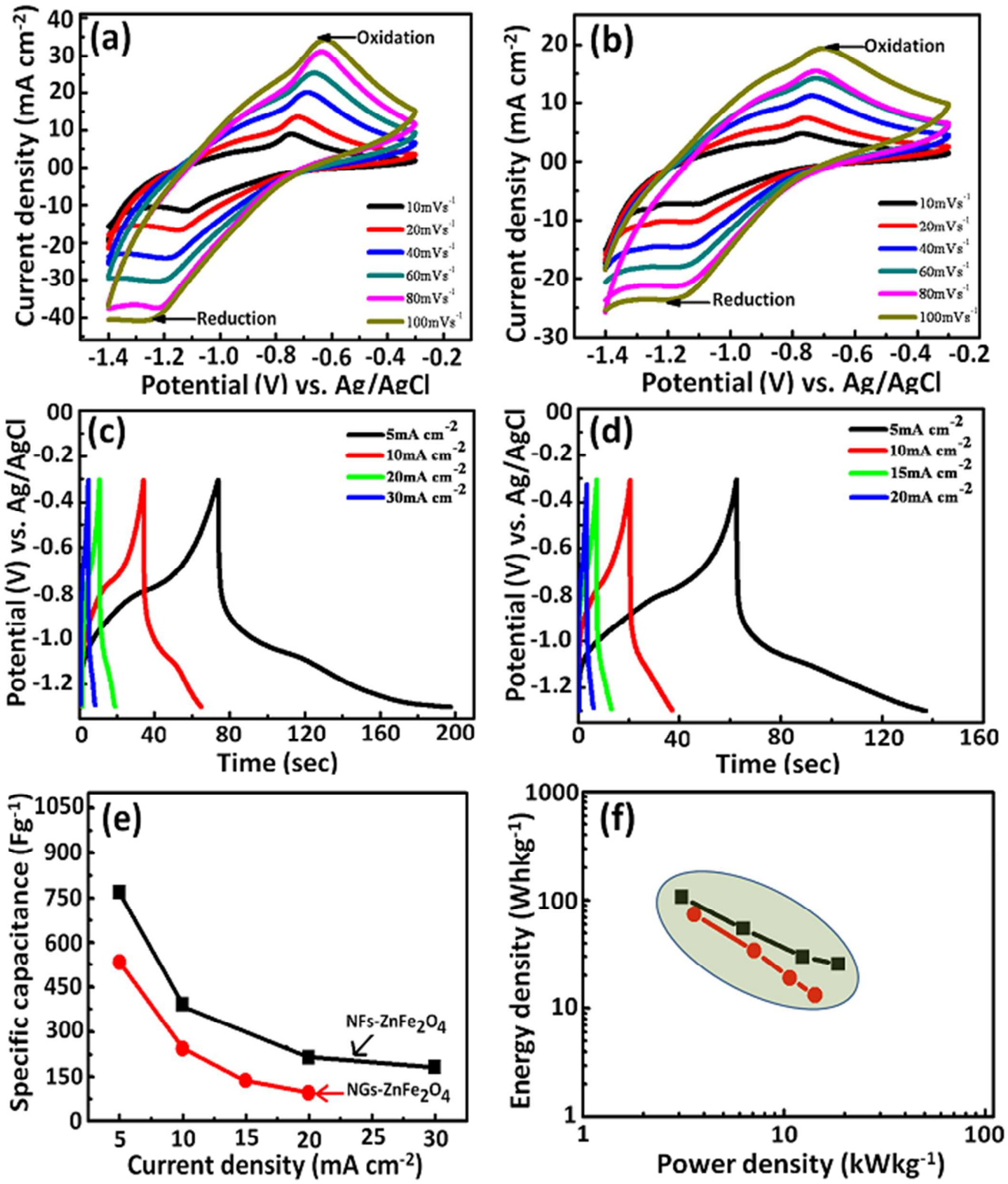

Fig. 7: (a) and (b) Cyclic Voltammograms (CV) at 10, 20, 40, 60, 80, 100 mVs^{-1} scan rates (c) and (d) Galvanostatic charge-discharge (GCD) curves of at 5, 10, 20, 30 mA cm^{-2} and 5, 10, 15, 20 mA cm^{-2} in 3M KOH electrolyte and (e) and (f) plot of current density (mA cm^{-2}) vs. Specific capacitance (Fg^{-1}) and Ragone plot of energy density vs. power density for NFs-$ZnFe_2O_4$ (Black) and NGs-$ZnFe_2O_4$ (Red) nanostructured thin films.

Table T1. Summary of electrochemical measurements reported in recent papers using MFe_2O_4 (M= Co, Cu, Mn, Fe) as supercapacitor electrodes

Sr. no.	Method	Nature of ferrite films	Structure	Current collector	Electrolyte with molar concentration	Maximum capacitance Fg^{-1}	Current density $mA.cm^{-2}$ or Scan rate $mV.s^{-1}$	References (year)
1	Precipitation	$MnFe_2O_4$ powder	Granular	Platinum mesh	1M NaCl	100 Fg^{-1}	10 mV/s	(2005)[12]
2	Hydrothermal	$NiFe_2O_4$/graphene powder	Particles	Platinum electrode	1M Na_2SO_4	345 Fg^{-1}	1 Ag^{-1}	(2013)[34]
3	Chemical bath deposition	$CoFe_2O_4$ Thin film	Nano-flakes	Graphite	1M Na_2SO_4	366 Fg^{-1}	10 mV/s	(2012)[9]
4	Solvothermal	$CuFe_2O_4$ powder	Nanospheres	Platinum wire	1M KOH	334 Fg^{-1}	0.6 Ag^{-1}	(2013)[13]
5	Hydrothermal	$CoFe_2O_4$ Thin film	Nano-flowers	Platinum plate	1M KOH	768 Fg^{-1}	$6Ag^{-1}$	(2015)[36]
6	**Chemical bath deposition**	**$ZnFe_2O_4$ Thin film**	**Nano-flakes** / **Nano-grains**	**Graphite**	**3M KOH**	**768 Fg^{-1}** / **534 Fg^{-1}**	**5 mA cm^{-2}**	**Present work**

Graphical Abstract

Mechanochemical Growth of Porous $ZnFe_2O_4$ Nano-flakes Thin Film as Electrode for Supercapacitor Application

M. M. Vadiyar,[a] S. C. Bhise,[a] S. K. Patil,[a] S. A. Patil,[a] D. K. Pawar,[a] A. V. Ghule,[b*] P. S. Patil[c] and S. S Kolekar[a]*

[a]Analytical Chemistry and Material Science Research Laboratory, Department of Chemistry, Shivaji University, Kolhapur 416004, Maharashtra, India. E-mail: sskolekar@gmail.com
[b]Green Nanotechnology Laboratory, Department of Chemistry, Shivaji University, Kolhapur 416004, Maharashtra, India E-mail: anighule@gmail.com
[c]Thin Film Materials Laboratory, Department of Physics, Shivaji University, Kolhapur 416 004, India.

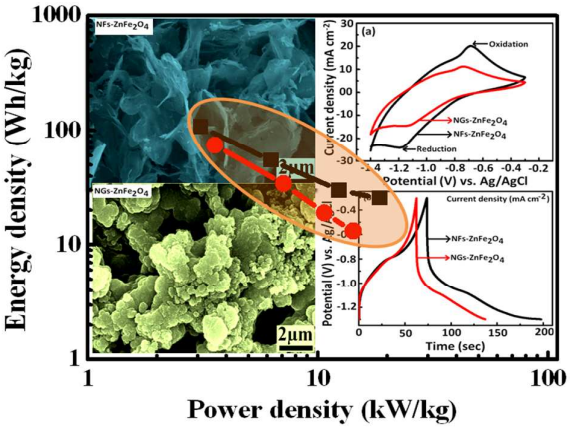

$ZnFe_2O_4$ nano-flakes thin films prepared using mechanochemical approach for supercapacitor application showing excellent specific capacitance, stability, energy and power density.